

# Sodiation and Desodiation via Helical Phosphorus Intermediates in High-Capacity Anodes for Sodium-Ion Batteries

Marbella, Lauren E.; Evans, Matthew L.; Groh, Matthias F.; Nelson, Joseph; Griffith, Kent J.; Morris, Andrew; Grey, Clare P.

DOI:

[10.1021/jacs.8b04183](https://doi.org/10.1021/jacs.8b04183)

License:

Creative Commons: Attribution (CC BY)

*Document Version*

Publisher's PDF, also known as Version of record

*Citation for published version (Harvard):*

Marbella, LE, Evans, ML, Groh, MF, Nelson, J, Griffith, KJ, Morris, A & Grey, CP 2018, 'Sodiation and Desodiation via Helical Phosphorus Intermediates in High-Capacity Anodes for Sodium-Ion Batteries', *Journal of the American Chemical Society*, vol. 140, no. 25, pp. 7994–8004. <https://doi.org/10.1021/jacs.8b04183>

[Link to publication on Research at Birmingham portal](#)

## General rights

Unless a licence is specified above, all rights (including copyright and moral rights) in this document are retained by the authors and/or the copyright holders. The express permission of the copyright holder must be obtained for any use of this material other than for purposes permitted by law.

- Users may freely distribute the URL that is used to identify this publication.
- Users may download and/or print one copy of the publication from the University of Birmingham research portal for the purpose of private study or non-commercial research.
- User may use extracts from the document in line with the concept of 'fair dealing' under the Copyright, Designs and Patents Act 1988 (?)
- Users may not further distribute the material nor use it for the purposes of commercial gain.

Where a licence is displayed above, please note the terms and conditions of the licence govern your use of this document.

When citing, please reference the published version.

## Take down policy

While the University of Birmingham exercises care and attention in making items available there are rare occasions when an item has been uploaded in error or has been deemed to be commercially or otherwise sensitive.

If you believe that this is the case for this document, please contact [UBIRA@lists.bham.ac.uk](mailto:UBIRA@lists.bham.ac.uk) providing details and we will remove access to the work immediately and investigate.

# Sodiation and Desodiation via Helical Phosphorus Intermediates in High-Capacity Anodes for Sodium-Ion Batteries

Lauren E. Marbella,<sup>†</sup> Matthew L. Evans,<sup>‡</sup> Matthias F. Groh,<sup>†</sup> Joseph Nelson,<sup>‡</sup> Kent J. Griffith,<sup>†</sup> Andrew J. Morris,<sup>\*,§</sup> and Clare P. Grey<sup>\*,†</sup>

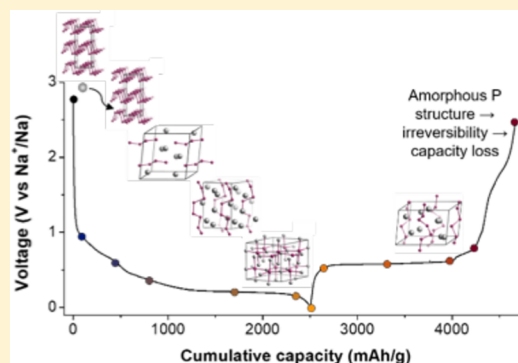
<sup>†</sup>Department of Chemistry, University of Cambridge, Lensfield Road, Cambridge CB2 1EW, United Kingdom

<sup>‡</sup>Theory of Condensed Matter Group, Cavendish Laboratory, University of Cambridge, J. J. Thomson Avenue, Cambridge CB3 0HE, United Kingdom

<sup>§</sup>School of Metallurgy and Materials, University of Birmingham, Edgbaston, Birmingham B15 2TT, United Kingdom

## S Supporting Information

**ABSTRACT:** Na-ion batteries are promising alternatives to Li-ion systems for electrochemical energy storage because of the higher natural abundance and widespread distribution of Na compared to Li. High capacity anode materials, such as phosphorus, have been explored to realize Na-ion battery technologies that offer comparable performances to their Li-ion counterparts. While P anodes provide unparalleled capacities, the mechanism of sodiation and desodiation is not well-understood, limiting further optimization. Here, we use a combined experimental and theoretical approach to provide molecular-level insight into the (de)sodiation pathways in black P anodes for sodium-ion batteries. A determination of the P binding in these materials was achieved by comparing to structure models created via species swapping, *ab initio* random structure searching, and a genetic algorithm. During sodiation, analysis of <sup>31</sup>P chemical shift anisotropies in NMR data reveals P helices and P at the end of chains as the primary structural components in amorphous Na<sub>x</sub>P phases. X-ray diffraction data in conjunction with variable field <sup>23</sup>Na magic-angle spinning NMR support the formation of a new Na<sub>3</sub>P crystal structure (predicted using density-functional theory) on sodiation. During desodiation, P helices are re-formed in the amorphous intermediates, albeit with increased disorder, yet emphasizing the pervasive nature of this motif. The pristine material is not re-formed at the end of desodiation and may be linked to the irreversibility observed in the Na–P system.



## INTRODUCTION

Na-ion batteries (NIBs) are promising alternatives for long-term sustainability in terms of both cost and natural abundance compared to Li-ion systems.<sup>1–5</sup> Na is widely available and evenly distributed worldwide, lessening the political tensions that may arise from continued Li use. While numerous viable cathode materials for NIBs have been identified from Li analogues,<sup>6,7</sup> many intercalation and alloying anode materials that work well for Li-ion batteries (LIBs) fail for Na chemistries. For example, the larger atomic size of Na does not allow intercalation into graphite<sup>8</sup> and the safety issues associated with microstructural formation are exacerbated when Na metal is used.<sup>9</sup> When exploring materials for high capacity anodes in NIBs, elemental phosphorus is an appealing option as it exhibits the highest theoretical capacity of any anode material that has been studied, the end member composition Na<sub>3</sub>P corresponding to a capacity of 2596 mA h g<sup>−1</sup>.<sup>8,10–13</sup> Due to the high natural abundance of P, the use of Na–P chemistries has the potential to further drive down the cost of NIBs while achieving performances comparable to those of LIBs. Such high performing phosphorus-containing batteries have potential use

in stationary systems, such as grid storage; we note, however, that the use of phosphorus anodes is associated with a safety risk—reduced phosphides can react with water, for example, to produce phosphine gas. However, with an emphasis on battery safety, monitoring tools, and quality assurance, the likelihood that these risks can be mitigated increases.

Initial reports showed that anodes composed of elemental P (both the red and black allotropes) and conductive carbon can elicit high capacities in NIBs (ranging from 1479–2077 mA h g<sup>−1</sup> reversible capacity in the first cycle).<sup>14–21</sup> Further improvements were achieved by using single-layer black P, i.e. phosphorene, in combination with graphene, which displayed a reversible capacity of 2440 mA h g<sup>−1</sup> in the first cycle.<sup>22</sup> Similarly high capacities are also observed in Li-ion systems for the formation of Li<sub>3</sub>P, allowing translation into existing LIB technology.<sup>16,23–29</sup> While these reports demonstrate the promise of P anodes for NIBs to offer high capacities competitive with LIBs, P-based anodes suffer from performance

Received: April 19, 2018

Published: June 19, 2018

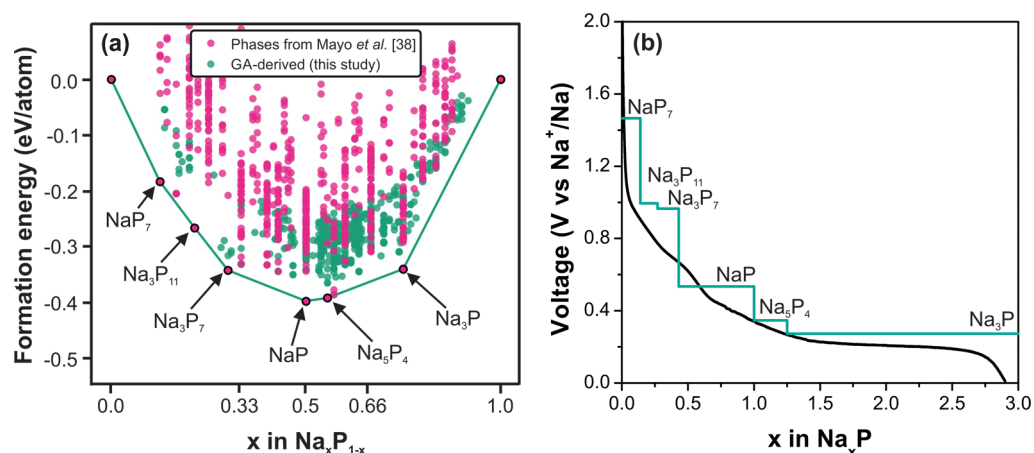


**Figure 1.** (a) Convex hull of  $\text{Na}_x\text{P}_{1-x}$  predicted with DFT energies of known, AIRSS, or species-swapping derived phases from ref 38 (magenta circles) and GA-derived phases (green circles). (b) Experimental (black, C-rate of C/100) and theoretical (teal) electrochemical profiles for the sodiation of black P. The electrochemical processes on the DFT-derived profile represent the formation of the following on-hull structures:  $\text{NaP}_7$  (1.47 V),  $\text{Na}_3\text{P}_{11}$  (0.99 V),  $\text{Na}_3\text{P}_7$  (0.96 V),  $\text{NaP}$  (0.53 V),  $\text{Na}_5\text{P}_4$  (0.35 V), and  $\text{Na}_3\text{P}$  (0.27 V).

issues such as low conductivity and capacity fade during cycling.<sup>30–33</sup>

Interpretation of electrochemical signatures relies on a thorough understanding of the chemistry that occurs on sodiation and desodiation. Thus, tracking the (de)sodiation pathways provides a platform with which to elucidate the structure–property relationships responsible for high capacities as well as to devise strategies to mitigate the performance degradation. Amine and co-workers<sup>19</sup> used *ex situ* and *in situ* synchrotron high-energy X-ray diffraction (XRD) to study electrochemical cycling of black P, and the only crystalline phases that were observed were the pristine material (orthorhombic black P) and crystalline  $\text{Na}_3\text{P}$  (*c*- $\text{Na}_3\text{P}$ ). No Bragg reflections were observed for any intermediate  $\text{Na}_x\text{P}$  ( $0 < x < 3$ ) compositions studied, indicating the lack of long-range ordering, consistent with the formation of amorphous/metastable phases (*a*- $\text{Na}_x\text{P}$ ;  $0 < x < 3$ ). Unlike other alloying anodes used in NIBs (e.g., Sn or Sb), P is a relatively light element and thus total scattering techniques such as pair distribution function (PDF) analysis of X-ray data, (which have been successfully used to aid structural assignment of both  $\text{Na}_x\text{Sn}$ <sup>34</sup> and  $\text{Na}_x\text{Sb}$ ,<sup>35</sup> both systems where disordered phases are observed along with crystalline phases) are difficult to model and interpret due to the relatively poor signal-to-noise ratio.<sup>36</sup> Conversely, NMR is well-suited to study the short-range order in the amorphous/metastable structures in *a*- $\text{Na}_x\text{P}$  due to the good sensitivities and 100% natural abundances of the NMR-active  $^{31}\text{P}$  and  $^{23}\text{Na}$  nuclei.

The Na–P composition space has previously been explored by some of the authors by using density functional theory (DFT) calculations to evaluate the formation energy of experimentally known  $\text{Na}_x\text{P}$  structures and new structure predictions derived from *ab initio* random structure searching (AIRSS) and structural prototyping (species swapping from known phases of similar compounds).<sup>38</sup> In similar systems, such *ab initio* structure searches have previously determined crystalline products not found in structure databases,<sup>34</sup> as well as identifying possible structural motifs present in disordered phases formed on cycling.<sup>39</sup> By the nature of AIRSS and prototyping, there is, however, no information flow between calculations, and thus these techniques are limited to the initial stoichiometries chosen at their outset.

Here, we show that by using a combination of solid-state NMR (ssNMR) and powder X-ray diffraction (PXRD) we can monitor the  $\text{Na}_x\text{P}$  phases that are formed on (de)sodiation in black P anodes. Specifically, individual P binding sites within the amorphous  $\text{Na}_x\text{P}$  phases that arise during cycling are probed with 2D  $^{31}\text{P}$  phase-adjusted spinning sideband (PASS) ssNMR experiments. In 2D PASS, isotropic shifts are correlated to the corresponding anisotropic chemical shifts, facilitating analysis of the full chemical shift (CS) tensors of individual P sites and ultimately providing information on the geometry of chemical bonding environments and structures of molecular fragments.<sup>37</sup> The crystalline structures that occur are characterized by  $^{31}\text{P}$  magic-angle spinning (MAS) ssNMR, variable field  $^{23}\text{Na}$  MAS ssNMR, and XRD. All experimental NMR and XRD data are interpreted through first-principles computational structure prediction.

In this current study, we move beyond the initial constrained AIRSS + prototype search and use a specialized variable-composition genetic algorithm (GA) code to interpolate to stoichiometries not sampled by the stochastic searches. Combining this theoretical approach with *ex situ* experimental analyses, we determine how P fragments in amorphous phases change during sodiation vs desodiation and show that the structure of the end member phase,  $\text{Na}_3\text{P}$ , is a phase previously computationally predicted using the AIRSS technique.<sup>38</sup>

## RESULTS

**Genetic Algorithm (GA) Sampling of Theoretical Predictions of  $\text{Na}_x\text{P}$  Structures.** The GA was initiated from low-lying AIRSS-derived phases to avoid the need to extrapolate to entirely new regions of composition space. Evaluating the fitness of child structures as a function of distance from the convex hull, the GA uncovered several motifs from less ordered phases that could not be sampled with any individual technique alone. These new motifs provided a vast library of possible P binding environments to evaluate as potential local environments and motifs that may arise in the amorphous  $\text{Na}_x\text{P}$  structures formed on cycling. These GA-derived phases were added to the previously constructed<sup>38</sup> convex hull of thermodynamically stable  $\text{Na}_x\text{P}$  structures in Figure 1a.

The pristine material, black P, is a layered structure that contains six-membered P rings. The known phosphorus-rich polyphosphide of  $\text{NaP}_7$ <sup>40</sup> was considered and found to lie on the convex hull. In  $\text{NaP}_7$ , one Na coordinates to each  $[\text{P}_7]$  subunit–phosphorus motifs that form infinite tubes arranged in helices about the  $c$  axis.<sup>40</sup> In previous work, Morris and co-workers found a series of structures containing P cages ( $\text{Na}_3\text{P}_{11}$  and  $\text{Na}_3\text{P}_7$  exhibit  $\text{P}_{11}$  and  $\text{P}_7$  cages, respectively) (where  $0 < x < 0.43$  in  $\text{Na}_x\text{P}$ ) that fall on the convex hull.<sup>38</sup> As the sodium content increases, the next on-hull phases are  $\text{NaP}$  and  $\text{Na}_3\text{P}_4$ , which exhibit P helices and four-member P zig-zags, respectively. At the end of sodiation, isolated P ions are found in  $\text{Na}_3\text{P}$ .

**Electrochemical Characterization and Comparison with Calculated Potentials.** The theoretical structure models (with energies depicted in Figure 1a) were compared to  $\text{Na}_x\text{P}$  phases that arise during cycling of black P in NIBs. Black P electrodes were assembled into Na half-cells for electrochemical measurements. Near-theoretical capacity was reached on the first discharge ( $2510 \text{ mA h g}^{-1}$ , based on the mass of P alone) and one of the highest reversible capacities observed to date of  $2074 \pm 80 \text{ mA h g}^{-1}$  without the use of additives is achieved in the first cycle. The improved capacity may be due to the use of 1.0 M NaFSI in 2-MeTHF as the electrolyte, which differs from the electrolytes used previously (1.0 M  $\text{NaClO}_4$  in EC/DMC or 1.0 M  $\text{NaPF}_6$  in PC). When compared to PC, methyl acetate, or THF, 2-MeTHF shows improved stability against  $\text{Li}$ ,<sup>41</sup> and similar stability is likely present toward Na, thus improving the electrochemical performance of the NIBs. The experimental P reduction profile was compared to the average voltages for on-hull  $\text{Na}_x\text{P}$  structures predicted by Morris and co-workers<sup>38</sup> (Figure 1b). When a constant current is applied (C/100), the voltage drops from the open circuit voltage to 1.10 V (Figure 1b). This initial voltage drop suggests that  $\text{P}_{11}$  and  $\text{P}_7$  subunits, such as those found in  $\text{NaP}_7$  and the computed structures of  $\text{Na}_3\text{P}_{11}$  and  $\text{Na}_3\text{P}_7$ , may not form electrochemically during sodiation in a NIB. Their absence may be due to the unfavorable energetics involved with breaking the six-membered P rings in black P and re-forming P–P bonds to form the  $\text{P}_{11}$  and/or  $\text{P}_7$  cages in these structures. Instead a sloping region is seen between 1.10 and 0.63 V, corresponding to  $31\text{--}420 \text{ mA h g}^{-1}$  and approximate compositions of  $\text{Na}_{0.04}\text{P}\text{--}\text{Na}_{0.49}\text{P}$ . A steep, but short-lived sloping region is observed from 1.10–0.48 V ( $420\text{--}562 \text{ mA h g}^{-1}$ , approximate compositions of  $\text{Na}_{0.50}\text{P}\text{--}\text{Na}_{0.65}\text{P}$ ); which is followed by a more shallow, sloping region from 0.48–0.22 V ( $562\text{--}1358 \text{ mA h g}^{-1}$ , approximate compositions of  $\text{Na}_{0.65}\text{P}\text{--}\text{Na}_{1.57}\text{P}$ ), implying gradual sodiation of  $\text{Na}_x\text{P}$  (where  $x$  ranges from 0.04 to 1.57) from 0.63 to 0.22 V. Following this, a plateau at 0.21 V (ranging from  $1358\text{--}2340 \text{ mA h g}^{-1}$ , where  $x$  corresponds to 1.57–2.70) is observed with a distinct peak in the  $dQ/dV$  plot (Figure S2), which is attributed to the formation of  $c\text{-Na}_3\text{P}$ .<sup>21</sup>

**Ex Situ  $^{31}\text{P}$  MAS NMR Spectra on Sodiation.** *Ex situ*  $^{31}\text{P}$  MAS NMR spectra were acquired at different stages of (de)sodiation to probe the structural features of various  $\text{Na}_x\text{P}$  phases (Figure 2) directly. The  $^{31}\text{P}$  MAS NMR spectrum collected in the first sloping region at 0.90 V ( $124 \text{ mA h g}^{-1}$ , approximate composition,  $\text{Na}_{0.14}\text{P}$ ) is nearly identical to that of the pristine material, with the exception that a weak peak at  $-227 \text{ ppm}$  emerges (see Figure S8 for a magnified version of Figure 2b). Assignment of this low frequency resonance is not obvious based on its isotropic  $^{31}\text{P}$  shift alone. However, we note that peaks in this region (ca.  $-220$  to  $-250 \text{ ppm}$ ) persist

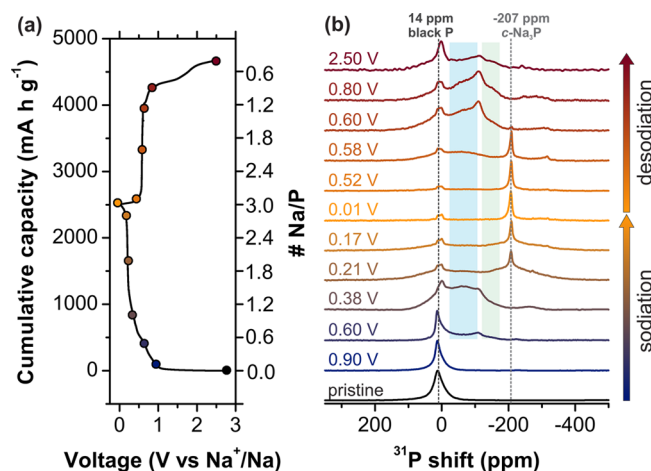


**Figure 2.** *Ex situ*  $^{31}\text{P}$  MAS NMR spectra (MAS = 60 kHz) of black P recorded at various stages of sodiation/desodiation (right) and the corresponding electrochemistry (left). The circles on the electrochemical profile indicate where cycling was arrested and samples were extracted for the NMR experiments. The  $^{31}\text{P}$  chemical shift of the pristine material, black P (dark gray, 14 ppm), and the final discharge product, crystalline  $\text{Na}_3\text{P}$  (light gray,  $-207 \text{ ppm}$ ) are shown in dashed lines.  $^{31}\text{P}$  chemical shift regions corresponding to P helical motifs and P near the end of chains are shaded in blue and green, respectively.

throughout all stages of (de)sodiation, suggesting this region arises from  $\text{Na}_x\text{P}$  species formed in side reactions, minor  $\text{Na}_x\text{P}$  intermediates or perhaps Na near P defects (such as the end of a P chain).

The  $^{31}\text{P}$  MAS NMR spectrum for the sample extracted at 0.60 V (approximate composition  $\text{Na}_{0.52}\text{P}$ ) spans a broad chemical shift range from the resonance of the pristine material (14 ppm) to the small, sharp peak at  $-224 \text{ ppm}$  (Figure 2b). Two pronounced broad peaks with centers-of-mass at  $-104$  and  $-143 \text{ ppm}$  are clearly resolved, these peaks becoming more pronounced as sodiation proceeds (Figure S8). The corresponding *ex situ* XRD pattern of this material does not show any Bragg reflections that are distinct from the pristine material (Figure S13) indicating that an amorphous or highly disordered phase is present in addition to residual black P. At 0.38 V ( $780 \text{ mA h g}^{-1}$ ; approximately  $\text{NaP}$ ;  $x = 1$ ), a broad set of resonances spanning a  $^{31}\text{P}$  chemical shift region from ca.  $-260$  to  $40 \text{ ppm}$  is again observed, along with the lack of Bragg reflections (Figure S13), suggesting that this phase is also amorphous ( $a\text{-Na}_x\text{P}$ ).

Following the formation of  $a\text{-Na}_x\text{P}$ , a sharp  $^{31}\text{P}$  resonance (fwhm = 10 ppm) emerges at  $-207 \text{ ppm}$  (Figure 2b) that is coincident with the plateau at 0.21 V in the electrochemical profile and is assigned to  $c\text{-Na}_3\text{P}$  on the basis of previous<sup>21</sup> (and current; see Supporting Information (SI)) *ex situ* XRD characterization at the corresponding state of charge. The set of broad  $^{31}\text{P}$  resonances decrease in intensity near the end of this plateau ( $1666 \text{ mA h g}^{-1}$ , approximate composition of  $\text{Na}_{1.93}\text{P}$ ) consistent with a two-phase reaction of  $a\text{-Na}_{3-x}\text{P}$  to  $c\text{-Na}_3\text{P}$  (where  $x$  is about 0.6; approximately composition  $a\text{-Na}_{2.4}\text{P}$ ), and vanish by the end of sodiation at 0.01 V ( $2510 \text{ mA h g}^{-1}$ , approximate composition of  $\text{Na}_{2.90}\text{P}$ ). Here  $x$  was quantified based on the capacity and integrating the area corresponding to the shifts of black P (14 ppm),  $c\text{-Na}_3\text{P}$  ( $-207 \text{ ppm}$ ), and assuming the integral of the remaining broad resonances corresponds to  $a\text{-Na}_{3-x}\text{P}$ .



**Assignment of the Crystal Structure of  $c$ - $\text{Na}_3\text{P}$  Formed at the End of Sodiation.** Previously, the crystallographic structure of  $\text{Na}_3\text{P}$  formed on discharge has been assigned as  $\text{Na}_3\text{P-P6}_3/\text{mmc}$  on the basis of both powder<sup>42</sup> and single crystal<sup>43</sup> XRD characterizations of solid state syntheses of  $\text{Na}_3\text{P}$ . However, our prior DFT calculations predicted a  $\text{P6}_3\text{cm}$  symmetry phase to be the most stable crystal structure of  $c$ - $\text{Na}_3\text{P}$  (i.e., located on the convex hull).<sup>38</sup> This phase was constructed via species swapping from the  $\text{Na}_3\text{As}$  structure<sup>44</sup> and can be rationalized as a distorted variant of a previously reported crystal structure of  $\text{Na}_3\text{P-P6}_3/\text{mmc}$ <sup>42,43</sup> which resides 0.005 eV-f.u.<sup>-1</sup> above the DFT hull.<sup>38</sup> These two structural models (Figure 3a) are closely related by a group–subgroup transition of the order 6 (Figure S17). In the  $\text{P6}_3\text{cm}$  structure, the  $\text{PNa}_5$  trigonal bipyramids are distorted and tilted, which can

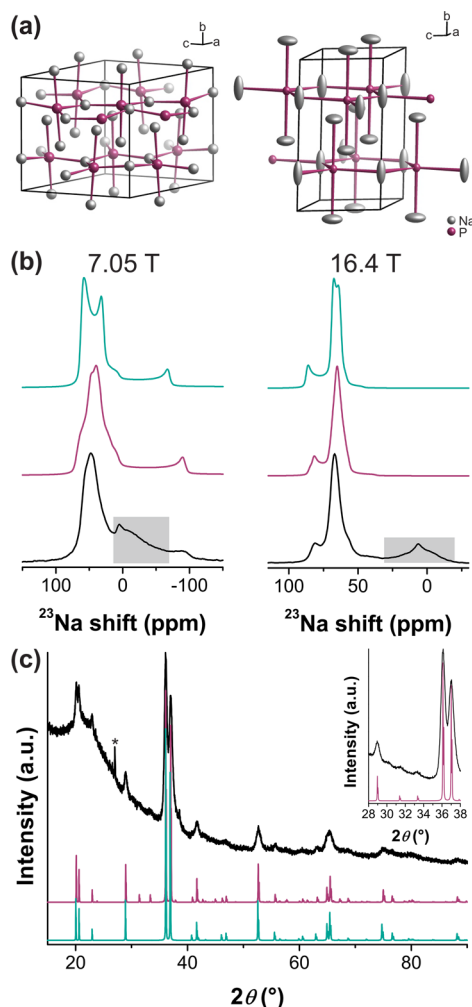


**Figure 3.** (a) Crystal structures of  $\text{Na}_3\text{P-P6}_3\text{cm}$  (left, calculated) and  $\text{Na}_3\text{P-P6}_3/\text{mmc}$  (right). (b)  $^{23}\text{Na}$  NMR (MAS = 60 kHz) of a sample extracted at the end of sodiation (0.01 V, 2510 mA h g<sup>-1</sup>, black, bottom) compared to calculated spectra of  $\text{Na}_3\text{P-P6}_3\text{cm}$  (purple, middle) and  $\text{Na}_3\text{P-P6}_3/\text{mmc}$  (teal, top) at 7.05 (left) and 16.4 T (right). The shaded  $^{23}\text{Na}$  peaks in the experimental spectra correspond to Na in the CMC binder, carbon mixture, and/or SEI (Figure S7). (c) PXRD patterns of NIBs (black, top) compared to calculated patterns for  $\text{Na}_3\text{P-P6}_3\text{cm}$  (purple, middle, refined model) and  $\text{Na}_3\text{P-P6}_3/\text{mmc}$  (teal, bottom). The asterisk at approximately 27,  $2\theta$  denotes the major reflection from KBr, which was used as an internal standard. Inset shows the region containing characteristic reflections for  $\text{Na}_3\text{P-P6}_3\text{cm}$ .

be interpreted as frozen vibrational motion of the  $\text{Na}_3\text{P-P6}_3/\text{mmc}$  crystal structure, consistent with the anisotropic displacement parameters. The simulated XRD pattern of  $\text{Na}_3\text{P-P6}_3\text{cm}$  shows additional reflections at 31.3° and 33.3° (Cu K $\alpha$ ) that are absent in the otherwise essentially identical pattern of  $\text{Na}_3\text{P-P6}_3/\text{mmc}$ . Examination of the XRD of  $\text{Na}_3\text{P}$  samples derived by sodiation of black P in the NIBs revealed similar superstructure reflections and thus lower symmetry (Figure 3c). In addition, we find that  $\text{Na}_3\text{P}$  synthesized using standard solid-state synthesis techniques in our laboratory also exhibits these superstructure reflections (Figure S16), consistent with the formation of  $\text{Na}_3\text{P-P6}_3\text{cm}$ . A Rietveld refinement starting from the calculated structure model was performed on both samples. The refined atomic parameters for the sample synthesized via solid state synthesis differ only marginally from those calculated with DFT (Table S2, Figures S14 and S16). The slightly larger deviation observed for  $\text{Na}_3\text{P}$  formed electrochemically is attributed to the broadening of the Bragg reflections and thus lower signal-to-noise ratio of the data (Figure S15).

Both structural models ( $\text{P6}_3/\text{mmc}$  and  $\text{P6}_3\text{cm}$ ) feature only one independent P position, with isolated P ions. DFT calculations of the corresponding  $^{31}\text{P}$  NMR shifts appear in a similar spectral region (−180 vs −217 ppm for  $\text{P6}_3\text{cm}$  vs  $\text{P6}_3/\text{mmc}$ , respectively) and fall on either side of the experimentally observed value (−207 ppm). Furthermore, both crystal structures show very little anisotropy based on computed CS tensor values (anisotropy,  $\Delta$  = 38 ppm and asymmetry parameter,  $\eta$  = 0.41 for  $\text{P6}_3\text{cm}$ ;  $\Delta$  = −39 ppm,  $\eta$  = 0 for  $\text{P6}_3/\text{mmc}$ ), making  $^{31}\text{P}$  NMR an inconclusive diagnostic for structural determination of this species in the NIBs. However, the reduction of symmetry from  $\text{P6}_3/\text{mmc}$  to  $\text{P6}_3\text{cm}$  results in four instead of two crystallographically independent Na environments—all of which exhibit characteristic  $^{23}\text{Na}$  quadrupolar coupling constants and asymmetry parameters (Table 1,  $C_Q$  and  $\eta$ , respectively). Comparison of the  $^{23}\text{Na}$

**Table 1.** Calculated  $^{23}\text{Na}$  NMR Parameters for  $\text{Na}_3\text{P}$  Structure Models

compound	Na site	$\delta_{\text{iso}}$ (ppm)	$C_Q$ (MHz)	$\eta$
$\text{Na}_3\text{P-P6}_3/\text{mmc}$	Na1	94	5.13	0
	Na2	70	−2.56	0
$\text{Na}_3\text{P-P6}_3\text{cm}$	Na1	93	5.50	0
	Na2	90	5.41	0
	Na3	71	−2.36	0.98
	Na4	69	−2.53	0.49

MAS NMR of the active materials at the end of sodiation (0.01 V, 2510 mA h g<sup>-1</sup>) to simulations of the  $^{23}\text{Na}$  spectra for both structures reveal significantly better agreement with the  $\text{Na}_3\text{P-P6}_3\text{cm}$  structure (Figure 3b), supporting the assignment of the formation of  $\text{Na}_3\text{P-P6}_3\text{cm}$  in NIBs.

**Structural Assignment of P Motifs in Amorphous  $\text{Na}_x\text{P}$  ( $x = 1$ ) During Sodiation.** With assignment of the crystallographic structure of the final discharge product in hand, the structures of the amorphous intermediates that form during (de)sodiation are now investigated in order to assign the observed  $^{31}\text{P}$  NMR resonances to specific local structures. [N.B.  $^{23}\text{Na}$  MAS NMR spectra were acquired for all the samples studied (Figure S6) and compared with DFT calculations of on-hull structures, but they were less informative than the  $^{31}\text{P}$  spectra (see SI).] NMR parameters for energetically low-lying

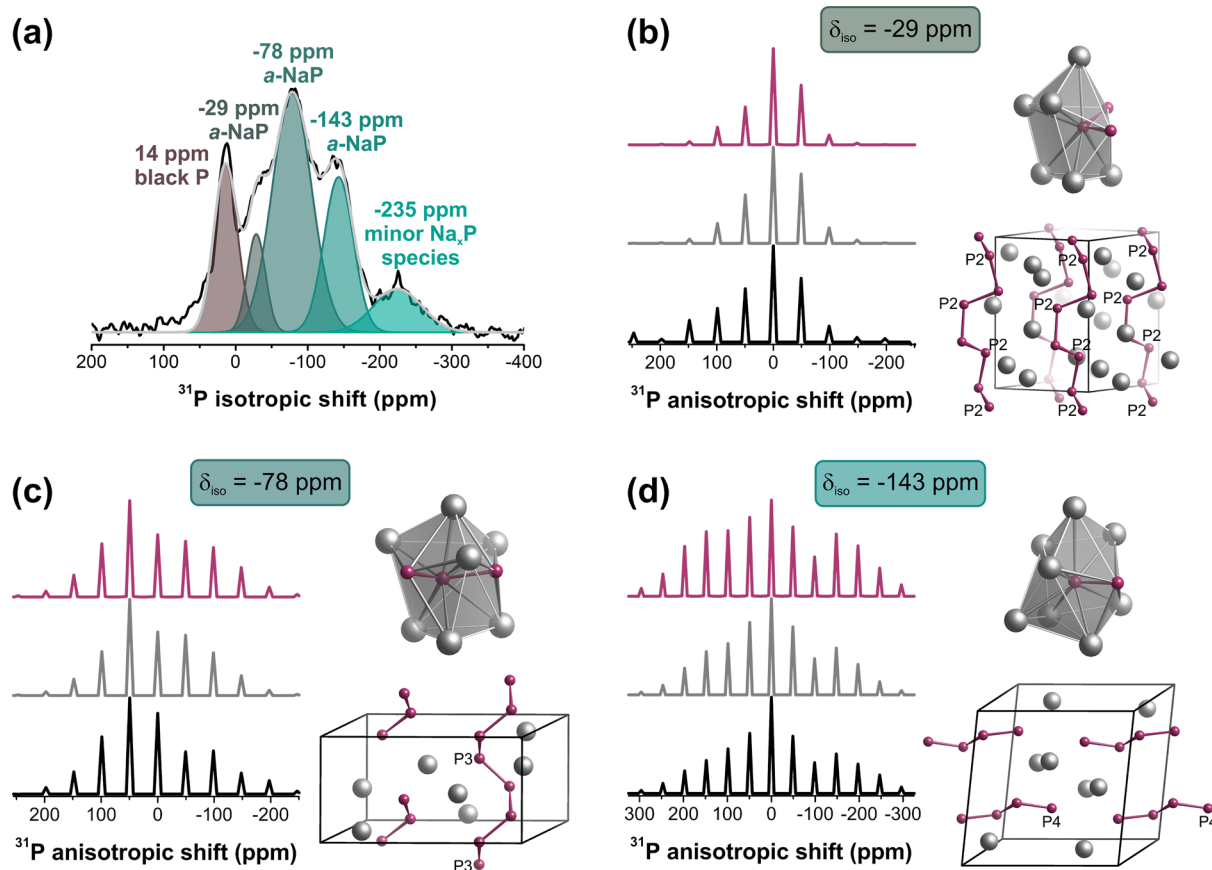


**Figure 4.** (a) Deconvolution of the  $^{31}\text{P}$  isotropic projection from 2D  $^{31}\text{P}$  PASS experiments (black line) performed on a sample of approximate composition NaP, extracted from a NIB at 0.38 V ( $780\text{ mA h g}^{-1}$ ) during sodiation. Five regions with centers-of-mass at 14 (black P),  $-29$ ,  $-78$ ,  $-143$ , and  $-235$  ppm are observed. The fit of the line shape from deconvolution is shown in gray. (b–d) Corresponding experimental anisotropic projections from 2D  $^{31}\text{P}$  PASS (black, bottom) showing sideband patterns for  $\delta_{\text{iso}} = -29$  (b),  $-78$  (c), and  $-143$  ppm (d) with the respective fits (middle, gray) compared to sideband patterns calculated for individual P sites in DFT models (top, purple) at MAS = 10 kHz. The corresponding P sites (top) and extended P structures (bottom) are displayed to the right of each sideband pattern and are listed in Table 2.

compositions corresponding to stoichiometries at or near  $\text{Na}_1\text{P}_1$  ( $\text{NaP}$ ,  $\text{Na}_5\text{P}_6$ ,  $\text{Na}_5\text{P}_4$ ,  $\text{Na}_7\text{P}_8$ ,  $\text{Na}_8\text{P}_7$ ) were first calculated (Figure S12). The structural diversity computationally accessed in this composition range from known, AIRSS, prototype, and GA-derived structures allows us to sample the  $^{31}\text{P}$  site variation that may be observed in the amorphous  $\text{Na}_x\text{P}$  phases more fully. Unfortunately, the  $^{31}\text{P}$  isotropic shifts calculated for these structural models were associated with a narrow spectral range, or the materials themselves did not exhibit a bandgap (which did not allow us to calculate accurate values for  $\delta_{\text{iso}}$  because the Knight shift contribution that describes the influence of free carriers could not be computed), prohibiting assignment based on isotropic shift alone. However, we found that individual  $^{31}\text{P}$  sites within the structural models exhibited distinct differences in chemical shift anisotropies (CSAs). Therefore, local  $^{31}\text{P}$  environments in the  $a\text{-NaP}$  phase were examined in greater detail with 2D  $^{31}\text{P}$  PASS experiments to separate isotropic and anisotropic chemical shifts and thus enable analysis of the full CS tensors of individual P sites. 2D PASS is particularly useful here, not only because of ambiguity in the isotropic  $^{31}\text{P}$  dimension, but these spectra are also broadened by strong intramolecular  $^{31}\text{P}$ – $^{31}\text{P}$  dipolar interactions<sup>45</sup> – potential interferences that are eliminated in the anisotropic dimension in PASS.

Deconvolution of the  $^{31}\text{P}$  isotropic projection shows the presence of (at least) three environments with associated  $^{31}\text{P}$

shifts at  $-29$ ,  $-78$ , and  $-143$  ppm that correspond to  $a\text{-Na}_x\text{P}$  species (Figure 4a), (with anisotropic projections shown in Figure 4b–d), the width and asymmetry of the CSA patterns differing noticeably for the three resonances. Sideband patterns were simulated in dmfit<sup>46</sup> (Figure 4b–d, gray) and compared to those calculated for  $^{31}\text{P}$  sites in DFT models (Figure 4b–d, purple) with similar compositions (*vide supra*).

The  $^{31}\text{P}$  site at  $\delta_{\text{iso}} = -29$  ppm agrees well with the CS tensor found for one crystallographically independent P site (P2 of P1–P2) in a metastable phase of NaP + 96 meV above the hull (Figure 4b, Table 2), which contains P arranged in a 3-fold helix that winds through the Na network. (In general, we find that all P atoms that comprise helical fragments are bound to two P atoms and surrounded by four to six Na atoms.) The P1 site of this phase is associated with a chemical shift of  $-57$  ppm, and if present, would likely be obscured by the much more intense  $\delta_{\text{iso}} = -78$  ppm resonance. Similarly, the  $^{31}\text{P}$  environment at  $\delta_{\text{iso}} = -78$  ppm agrees with the CS tensor found for the third independent P site (P3, of P1–P7) in NaP + 75 meV above the hull that also contains P helices (Figure 4c, Table 2) but has very different CSA parameters. The  $^{31}\text{P}$  site at  $\delta_{\text{iso}} = -143$  ppm closely resembles that of the fourth independent P site (P4, of P1–P8) in a second NaP structure + 96 meV above the hull, found via GA (Figure 4d and Table 2), this site corresponding to a terminal unit of a four-member P zig-zag motif, suggesting that this site represents a terminal

**Table 2. Comparison of the Experimental  $^{31}\text{P}$  CS Tensors Obtained for the “NaP” Sample Extracted at 0.38 V during Sodiation and Calculated CS Tensor Parameters for Individual  $^{31}\text{P}$  Sites in Structural Models with Stoichiometries at or near NaP**

$^{31}\text{P}$ site/compound	$\delta_{\text{iso}}$ (ppm)	$\Delta$ (ppm)	$\eta$
experimental	−29	179	0.72
P2 in NaP + 96 meV above hull <sup>a</sup>	−21	171	0.55
experimental	−78	−261	0.75
P3 in NaP + 75 meV above hull <sup>b</sup>	−109	−291	0.71
experimental	−143	−432	0.87
P4 in NaP + 96 meV above hull <sup>b</sup>	92 <sup>c</sup>	−438	0.85

<sup>a</sup>Structural model was found using AIRSS. <sup>b</sup>Model was found using GA. <sup>c</sup>Model does not exhibit a bandgap, and the Knight shift contribution to the isotropic shift was not calculated.

unit of a P chain (i.e., site of P–P bond cleavage). Although there are exceptions,  $\Delta$  is generally larger for sites at the end of P chains or in small clusters, in all the calculated structures examined, again supporting this assignment. It is important to stress that we do not believe that the various crystalline structures are formed, simply that CSA parameters consistent with terminal and helical structures appear to be present in the amorphous phase. We note that (in contrast to the one pulse spectra (Figure 2b) a well-defined peak for  $\delta_{\text{iso}} = -104$  ppm is not observed in the isotropic projection from 2D PASS. The absence of this and other possible resonances may be due to short spin–spin ( $T_2$ ) relaxation (all sites show  $T_2$  values <1 ms) with respect to the rotor period (100  $\mu\text{s}$ ) that significantly lowers the signal over the course of the five consecutive  $\pi$  pulses that are applied during the PASS experiment. Thus, while we can identify individual  $^{31}\text{P}$  sites from different structural models that show similar CS tensors to the experimental PASS data, the remaining sites in these helical units may also not be observed due to fast  $T_2$  relaxation and subsequent dephasing and/or overlap in the isotropic projection.

Similar, broad  $^{31}\text{P}$  shifts near −29, −78, and −143 ppm remain in the  $^{31}\text{P}$  MAS NMR spectra during further sodiation

(Figure 2b). Specifically, the resonance near −143 ppm increases in intensity relative to the other broad peaks (Figure S8), suggesting further fragmentation of P helices as more Na is added to the system. Analysis of the chemical shift tensor for the site at −235 ppm at 0.38 V (780 mA h g<sup>−1</sup>; approximately NaP;  $x = 1$ , *vide infra*) reveals a small anisotropy value ( $\Delta = 93$  ppm, Figure S11) that is similar to the isotropic  $^{31}\text{P}$  shifts and anisotropies associated with isolated P ions (e.g.,  $\delta_{\text{iso}} = -180$  ppm,  $\Delta = 38$  ppm for  $P6_3cm$  and  $\delta_{\text{iso}} = -217$  ppm,  $\Delta = -39$  ppm for  $P6_3/mmc$ ).

**Structural Assignment of P Motifs in  $\alpha\text{-Na}_x\text{P}$  ( $x = 1$ ) during Desodiation.** During desodiation, the  $c\text{-Na}_3\text{P-P}6_3cm$   $^{31}\text{P}$  resonance at −207 ppm persists during desodiation until >0.60 V (>1490 mA h g<sup>−1</sup>, approximate composition of  $\text{Na}_{1.28}\text{P}$ ), allowing the assignment of the disappearance of  $c\text{-Na}_3\text{P}$  to the peak at 0.60 V in the dQ/dV plot (Figure S2). 2D  $^{31}\text{P}$  PASS experiments were again performed on the NaP ( $x = 1$ ) stoichiometry sample (0.80 V, 1730 mA h g<sup>−1</sup>), for comparison to the P environments in  $\alpha\text{-NaP}$  formed on sodiation. The  $^{31}\text{P}$  peak at  $\delta_{\text{iso}} = -143$  ppm exhibits lower intensity in the isotropic projection (Figure S9), compared to the MAS spectrum (Figure S8), indicating a change in the  $T_2$  relaxation behavior of this  $^{31}\text{P}$  site on desodiation and/or overlap with a site that exhibits shorter  $T_2$  relaxation. The sideband pattern from 2D PASS for  $\delta_{\text{iso}} = -143$  ppm could not be reliably simulated with a single CSA pattern (Figure S10); this may be due to overlapping  $^{31}\text{P}$  sites at this frequency and/or increased structural disorder (either motional or static). These data suggest that although a clear  $^{31}\text{P}$  peak is observed at −143 ppm in the NMR spectra collected at 0.60 and 0.80 V (1490 and 1730 mA h g<sup>−1</sup>, Figure 2b) on desodiation, this may be due to different P sites that exhibit fortuitous overlap at this chemical shift and/or that P atoms at the end of a chain may exhibit more variation in coordination environment.

The remaining  $^{31}\text{P}$  sideband patterns from 2D PASS experiments on  $\alpha\text{-NaP}$  (0.8 V, 1730 mA h g<sup>−1</sup>, approximately NaP) during desodiation can again be correlated with P motifs in the structural models (Figure 5 and Table 3), the environments with  $\delta_{\text{iso}} = -29$  ppm and −78 ppm again showing reasonable agreement with NaP structures containing helices. The CSA parameters, while similar to those observed

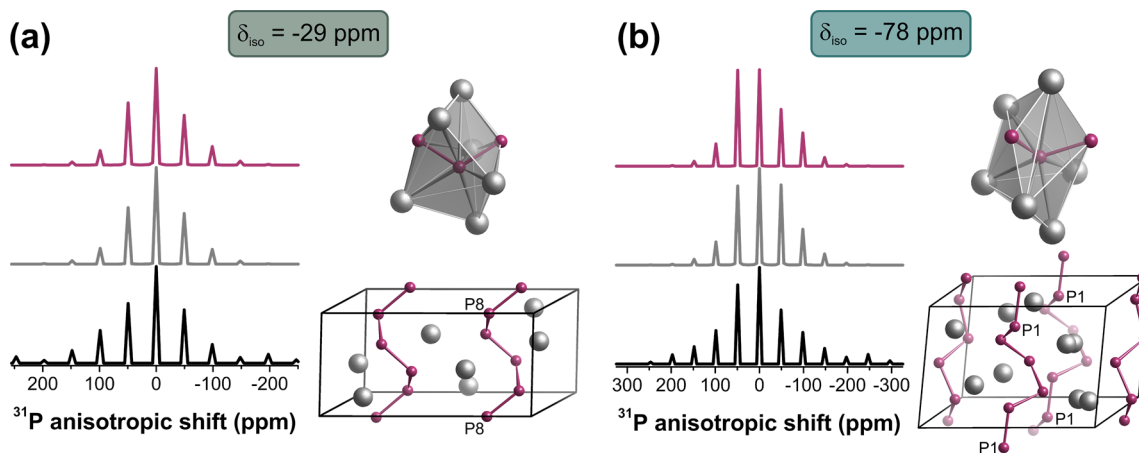


**Figure 5.** Experimental anisotropic projections from 2D  $^{31}\text{P}$  PASS (black, bottom) of NIBs at 0.80 V (1730 mA h g<sup>−1</sup>) during desodiation showing sideband patterns for  $\delta_{\text{iso}} = -29$  (a) and −78 ppm (b) with the respective fits (middle, gray) compared to sideband patterns calculated for individual P sites in DFT models (top, purple) at MAS = 10 kHz. The corresponding P sites (top) and extended P structures (bottom) are displayed to the right of each sideband pattern and are listed in Table 3.



**Table 3. Comparison of the Experimental  $^{31}\text{P}$  CS Tensors Obtained for  $\text{Na}_x\text{P}$  at 0.80 V (1730 mA h g $^{-1}$ ) during Desodiation and Calculated CS Tensor Parameters for Individual  $^{31}\text{P}$  Sites in Structural Models with Stoichiometries at or near NaP**

$^{31}\text{P}$ site/compound	$\delta_{\text{iso}}$ (ppm)	$\Delta$ (ppm)	$\eta$
experimental	−29	−163	0.95
P8 $\text{Na}_7\text{P}_8$ + 38 meV above hull <sup>a</sup>	150 <sup>b</sup>	−173	0.79
experimental	−78	−197	0.88
P1 NaP + 89 meV above hull <sup>a</sup>	−184	−205	0.59
experimental <sup>c</sup>	−143	−459	0.61
P2 $\text{Na}_7\text{P}_8$ + 55 meV above hull <sup>a</sup>	306 <sup>b</sup>	−462	0.65

<sup>a</sup>Structural model was found using GA. <sup>b</sup>Model does not exhibit a bandgap, and the Knight shift contribution to the isotropic shift was not calculated. <sup>c</sup>Simulation does not accurately represent experimental data due to spectral overlap.

on sodiation, are closer to those of structures with longer average Na–P interatomic distances (see SI for an expanded description of the structure models). Increased structural disorder on desodiation may be due to a larger range of clusters that are formed from the isolated P ions in  $\text{Na}_3\text{P}$ , as opposed to the original P phase, which already contains P–P bonds. At the end of desodiation at 2.5 V, a  $^{31}\text{P}$  shift (2 ppm) close to that of the pristine material (14 ppm) reemerges but is present alongside broad  $^{31}\text{P}$  resonances that span from 2 to −240 ppm (Figure 2b), indicating that the Na ions are not completely removed during desodiation and/or are consumed in deleterious side reactions. *Ex situ* XRD collected at the end of sodiation shows that black P is not re-formed (Figure S13). Rather, only one reflection at 26° that is also seen in *c*-black P is observed, suggesting that the material becomes increasingly amorphous during cycling.

## DISCUSSION

From the experimental and theoretical data presented, we propose a mechanism for sodiation/desodiation in phosphorus anodes for NIBs.  $^{31}\text{P}$  NMR spectra acquired during the initial stages of sodiation ( $\text{Na}_x\text{P}$ ,  $x = 0.14$ ) are similar to those of the pristine material, consistent with DFT calculations performed by Hembram et al.<sup>47</sup> which showed that the P–P bonds remained intact at low levels of sodiation ( $x < 0.25$ ). Only the interlayer distances increase, allowing Na ion intercalation prior to alloying and fragmentation of black P. The  $\text{P}_{11}$  and  $\text{P}_7$  cages present in on-hull  $\text{Na}_x\text{P}$  phases are not observed here, likely due to the energetic penalty associated with breaking/re-forming P–P bonds required to make P cages. Importantly, our  $^{31}\text{P}$  NMR spectra at early stages of sodiation do not resemble those reported for  $\text{NaP}_7$ , which shows four  $^{31}\text{P}$  resonances at −32.9, 20.6, 30.5, and 68.5 ppm that arise from the four independent  $^{31}\text{P}$  sites in this compound.<sup>40</sup> Once the composition reaches approximately  $\text{Na}_{0.52}\text{P}$ ,  $^{31}\text{P}$  NMR shifts consistent with P helices/zig-zags are present, suggesting that at this stage, the initial P–P cleavage has occurred, and P helices are the predominant structural motifs that are subsequently formed. P helices and zig-zags (which are likely truncated helices) may allow some of the original alternating planar/staggered P–P bonds found in pristine black P to persist while also forming an energetically favorable  $\text{Na}_x\text{P}$  phase.

As black P is further sodiated, the amorphous  $\text{Na}_x\text{P}$  phase that forms at 0.38 V (780 mA h g $^{-1}$ , approximate composition of NaP) shows  $^{31}\text{P}$  sites consistent with P helices and terminal P units from short P chains (four-member P zig-zags). The calculated voltage profile is in agreement with the measured experimental profile for  $x > 0.5$ , again confirming that the structural (helical) motifs found in structures such as NaP and  $\text{Na}_5\text{P}_4$  close to the convex hull are likely present.

Crystalline  $\text{Na}_3\text{P}$  emerges during a two-phase reaction that occurs below 0.22 V, suggesting that isolated P ions are derived from the P helices and shortened P chains (which increase in intensity in samples extracted during the two-phase reaction, Figures 2b and S8). A new crystalline architecture of  $\text{Na}_3\text{P}$  ( $\text{P6}_3\text{cm}$ ) was discovered from species swapping with  $\text{Na}_3\text{As}$  that is more thermodynamically stable than the previously determined  $\text{Na}_3\text{P-P6}_3/\text{mmc}$  structure found in two independent reports.<sup>42,43</sup> Theoretical calculations, variable field  $^{23}\text{Na}$  NMR, and XRD are consistent with the formation of this phase in a NIB and in solid-state syntheses performed in our laboratory. Crystalline  $\text{Na}_3\text{P}$  persists in the batteries during desodiation until a potential >0.6 V (>1490 mA h g $^{-1}$ ) is reached. In the *a*-NaP phase accessed during desodiation at 0.80 V (1730 mA h g $^{-1}$ ), more disordered P helices are found, perhaps due to the increased structural disorder associated with forming helices from isolated P ions in *c*- $\text{Na}_3\text{P-P6}_3\text{cm}$ . Black P does not re-form on Na removal from the system, and this irreversible chemistry may play a role in the poor capacity retention.

The prevalence of P helices in *a*-NaP during sodiation/desodiation indicates that this motif is ubiquitous in amorphous/metastable  $\text{Na}_x\text{P}$  structures. Four-fold P helices are present in *c*-NaP,<sup>48</sup> which falls on the convex hull tie-line, suggesting that this structural motif is conserved in the amorphous analogue, where more disorder and thus, lower symmetry is found. Calculations show that the higher symmetry *c*-NaP is associated with similar isotropic and anisotropic shifts for both independent  $^{31}\text{P}$  sites in the structure (P1,  $\delta_{\text{iso}} = -179$  ppm,  $\Delta = 288$  ppm, and  $\eta = 0.40$ ; P2,  $\delta_{\text{iso}} = -145$  ppm,  $\Delta = 292$  ppm, and  $\eta = 0.59$ ), neither of which accurately represent the experimental data, suggesting that lower symmetry/more disordered helices are present. DFT calculations by Hembram et al.<sup>47</sup> suggested that P dumbbells are formed at a composition of  $\text{Na}_{0.28}\text{P}$  that continue to increase in quantity until individual P ions are observed in  $\text{Na}_3\text{P}$ . In other Li-<sup>39,49–51</sup> and Na-ion<sup>34,35</sup> Sn, Ge and Si alloying anodes, dumbbell motifs are commonly observed in the amorphous phases formed on cycling. Conversely, our calculations show that the lowest lying structure of  $\text{Na}_x\text{P}$  ( $x = 2$ ) that exhibits dumbbells falls +54 meV above the hull, indicating that dumbbell-containing structures are less stable in the Na–P system. To determine whether dumbbell motifs were also formed during the (de)sodiation of black P, we compared the experimental CS tensors to those found for P–P dumbbells in  $\text{Na}_2\text{P}$  models with calculated energies ranging from +54 to +199 meV above the hull: while dumbbell motifs are associated with similar asymmetry parameters and sign of anisotropy for some of the  $^{31}\text{P}$  sites found on sodiation, the magnitude of the anisotropy is consistently smaller for the dumbbell motifs than those observed experimentally and the isotropic shift values deviate dramatically (e.g., experimental values for  $\delta_{\text{iso}} = -29$  ppm,  $\Delta = 179$  ppm, and  $\eta = 0.72$  whereas a dumbbell motif exhibits calculated values of  $\delta_{\text{iso}} = -246$  ppm,  $\Delta = 171$  ppm, and  $\eta = 0.68$ , ultimately indicating better agreement with the P site in helices with  $\delta_{\text{iso}} = -21$  ppm,  $\Delta = 171$  ppm, and  $\eta = 0.55$ , Table



S1). The lack of experimental evidence combined with the unfavorable formation energies of  $\text{Na}_2\text{P}$  structures indicates that dumbbell-containing structures do not form in a measurable quantity in these NIBs during cycling. Conversely, the CS tensor for  $\delta_{\text{iso}} = -143$  ppm is consistent with the terminal P atom in a four-member zig-zag motif, suggesting that this environment may represent the P–P cleavage site of a helix/zig-zag.

## CONCLUSION

Overall, we followed the structural transformations that occur during cycling in high capacity black P anodes for NIBs with solid-state NMR, XRD, and DFT calculations, providing insight into the (de)sodiation pathway. In tracking the various  $\text{Na}_x\text{P}$  intermediates that formed on cycling, the discovery of new  $\text{Na}_x\text{P}$  structures via the GA was crucial to assigning the P motifs present in  $a\text{-Na}_x\text{P}$  intermediates and AIRSS + prototyping structure searches allowed the assignment of the final discharge product.

During the first sodiation, P atoms at the end of a chain are observed as early as 0.60 V ( $\text{Na}_{0.52}\text{P}$ ), indicating that P–P cleavage begins at this composition. In  $a\text{-Na}_x\text{P}$ , P motifs that correspond to both P helices and the terminal unit in P zig-zags are observed, suggesting a sodiation mechanism that is distinct from other alloying anodes including other group 15 elements, e.g. Sb,<sup>35</sup> in which dumbbells are present. Once the potential drops below 0.22 V, the formation of a lower energy  $c\text{-Na}_3\text{P-P6}_3\text{cm}$  structure, which was predicted to form *a priori*, appears and persists during desodiation until >0.60 V. By comparing the product formed at the end of sodiation in NIBs with traditional solid-state synthesis, we find that the crystalline architecture is  $\text{Na}_3\text{P-P6}_3\text{cm}$  in both cases, indicating that both routes access the thermodynamically favorable structure. Slight differences in P environments in  $a\text{-NaP}$  during sodiation/desodiation may result from different pathways that are accessed to form extended P structures from the pristine black P vs the isolated P atoms in  $c\text{-Na}_3\text{P-P6}_3\text{cm}$ , respectively. At the end of desodiation, we find that black P is not re-formed, which may contribute to the poor capacity retention in this material. The combined approach of analyzing both experimental and theoretical CSA can be extended to understand other structural transformations on (de)lithiation/(de)sodiation in not only phosphorus-containing materials, but also systems, such as Si, where distinct structural motifs, such as clusters and chains, play an important role in the battery chemistry of these largely amorphous phases.

## EXPERIMENTAL SECTION

**Materials.** Red phosphorus ( $\geq 99.99\%$ ), carbon nanotubes (multi-walled), graphite (99.95%), 2-methyl tetrahydrofuran (2-MeTHF, anhydrous,  $\geq 99.0\%$ ), sodium metal (cubes in mineral oil, 99.9%), hexane (anhydrous, 95%), and sodium carboxymethyl cellulose (NaCMC, DS = 0.7,  $M_w = 700\,000$ ) were purchased from Sigma-Aldrich. Carbon super P (Timcal, 99+%) was purchased from Alfa Aesar. Sodium(I) bis(fluorosulfonyl)imide (NaFSI, 99.7%) was purchased from Solvionic. Prior to use, NaFSI was dried at 100 °C under vacuum before transferring to an Ar-filled glovebox (M. Braun;  $p(\text{O}_2)/p^0 < 1$  ppm,  $p(\text{H}_2\text{O})/p^0 < 1$  ppm). All other reagents were used as received.

**Electrode Preparation.** Red phosphorus powder (400 mg, 13 mmol) was placed in a  $\text{ZrO}_2$  jar in an Ar-filled glovebox and ball-milled using a SPEX 8000 M mixer/mill for 4 h to produce crystalline black phosphorus. To make the electrodes, black P was combined with conductive carbon for a final mass ratio of P:C = 50:50 (where C = 15

graphite:10 carbon nanotubes:10 carbon super P:15 NaCMC). First, black P was mixed with graphite, carbon nanotubes, and carbon super P in a  $\text{ZrO}_2$  jar and ball-milled for 1 h under Ar. After ball-milling, NaCMC in water was added to the P:C mixture to form an aqueous slurry which was cast onto etched Cu foil with a 150  $\mu\text{m}$  doctor blade. The resulting film was dried in air overnight, followed by drying at 100 °C under vacuum for an additional 12 h. Supported black P electrodes for assembly in coin cells were made using a 12.7 mm diameter circular punch and used for all electrochemical measurements and *ex situ* characterization studies with NMR and XRD. Typical loading values of active material were 1–3 mg of black P per electrode.

**Electrochemical Measurements.** Black P electrodes were assembled into Na half-cells using R2032 coin cells in an Ar-filled glovebox. The electrolyte used for all measurements was 1.0 M NaFSI dissolved in 2-MeTHF. Black P and metallic Na were separated with a glass fiber separator (Whatman, GF/A). All electrochemical measurements were performed using a Biologic MPG2 battery cycler. Cells were galvanostatically cycled in the potential range of 2.5 to 0.01 V at a rate of C/100, unless otherwise noted. C-rate is defined as the inverse of the number of hours it takes to reach a defined theoretical capacity—in this case, 2596 mA h  $\text{g}^{-1}$ .

**Solid-state NMR Spectroscopy.** For *ex situ* NMR measurements, black P electrodes were cycled against Na in half-cells to various states of charge. Batteries were disassembled in an Ar-filled glovebox and active materials were scraped off the Cu foil and washed twice with 2-MeTHF before drying under vacuum for 30 min. The dried powder (approximately 3–8 mg of material) was packed into  $\text{ZrO}_2$  rotors for analysis with  $^{31}\text{P}$  and  $^{23}\text{Na}$  solid-state NMR. Dried powders filled 1.3 mm o.d. (2.5  $\mu\text{L}$  internal volume)  $\text{ZrO}_2$  rotors for fast MAS experiments. For 2D  $^{31}\text{P}$  PASS measurements, 3–8 mg of material from a single battery could not fill the entire volume of a 4 mm o.d.  $\text{ZrO}_2$  rotor (80  $\mu\text{L}$  internal volume). For these experiments, material collected from a single battery was center-packed using Teflon to fill the void space.  $^{31}\text{P}$  and  $^{23}\text{Na}$  shifts were externally referenced to solid ammonium dihydrogen phosphate at 0.8 ppm and solid sodium chloride at 7.2 ppm, respectively.

Solid-state  $^{23}\text{Na}$  MAS NMR measurements were performed on Bruker Avance III 300 and 700 MHz spectrometers (operating at 7.05 and 16.4 T, respectively) equipped with a 1.3 mm HX MAS probehead.  $^{23}\text{Na}$  MAS NMR experiments were collected at MAS frequency = 60 kHz using a rotor-synchronized quadrupolar echo sequence and a recycle delay of 5 s ( $\geq 5 \times T_1$ ). Solid-state  $^{31}\text{P}$  MAS NMR measurements were performed on a Bruker Avance III 300 MHz spectrometer (7.05 T) equipped with a 1.3 mm HX probehead. Rotor-synchronized Hahn echo  $^{31}\text{P}$  MAS NMR experiments were collected at MAS frequency = 60 kHz with a recycle delay of 10 s (at least  $5 \times T_1$ ,  $T_1$  values ranged from hundreds of ms to approximately 2 s) [N.B. A recycle delay of 60 s was used for the pristine black P due to the longer spin–lattice relaxation time ( $T_1 = 9.5$  s) observed for this sample.]

2D  $^{31}\text{P}$  PASS NMR experiments were performed on a Bruker Avance III 500 spectrometer operating at 11.74 T and equipped with a 4 mm HXY MAS probehead. Spinning speeds of 10 kHz and recycle delays of 10 s were used for all PASS experiments. The PASS pulse sequence consists of a  $\pi/2$  pulse followed by a train of five rotor-synchronized  $\pi$  pulses with interpulse delays that satisfy the PASS equations.<sup>52</sup> For each experiment, the indirect dimension was incremented in 16 steps, with either 1200 or 2400 scans collected per step. All 2D data sets were processed by repeating the 2D signal in the indirect dimension eight times to separate spinning sidebands. All spinning sideband patterns were simulated in dmfit<sup>46</sup> to extract the principal components ( $\delta_{11}$ ,  $\delta_{22}$ , and  $\delta_{33}$ ) of the chemical shift tensor for comparison to DFT models. All chemical shift tensors reported here use the Haebleren–Mehring convention<sup>53</sup> to define the isotropic chemical shift ( $\delta_{\text{iso}}$ ), anisotropy ( $\Delta$ ), and asymmetry ( $\eta$ ) as follows:

$$\delta_{\text{iso}} = \left( \frac{\delta_{11} + \delta_{22} + \delta_{33}}{3} \right)$$

$$\Delta = \delta_{zz} - \frac{(\delta_{xx} - \delta_{yy})}{(2)} = \frac{3(\delta_{zz} - \delta_{iso})}{2}$$

$$\eta = \frac{(\delta_{yy} - \delta_{xx})}{(\delta_{zz} - \delta_{iso})}$$

In the Haeberlen convention, the principal components are defined as follows:

$$|\delta_{zz} - \delta_{iso}| \geq |\delta_{xx} - \delta_{iso}| \geq |\delta_{yy} - \delta_{iso}|$$

**X-ray Diffraction.** The air-sensitive Na<sub>3</sub>P powder samples were finely ground in an agate mortar, filled into 0.3 mm diameter glass capillaries, and sealed with two-component glue inside an Ar-filled glovebox. Diffraction data was collected at 296(2) K on a Panalytical Empyrean diffractometer equipped with a Ni filter using Cu K $\alpha$  radiation ( $\lambda$  = 154.06 pm, 154.43 pm). Rietveld refinement was performed using the TOPAS Academic software package (version 4.1).<sup>54</sup> Due to inadequate data quality, the displacement parameters of the atoms were fixed to  $U_{iso}$  = 0.013 pm<sup>2</sup>. In addition, the  $z$  parameter of one atom needed to be fixed owing to strong correlation. After individual refinement of each  $z$  parameter while one other was fixed,  $z(P1)$  was fixed for the last iteration. Interatomic distances should be treated with care due to the data quality. Crystal structures were visualized using the Diamond software package.<sup>55</sup>

Data in brief for Na<sub>3</sub>P at 296(2) K:  $a$  = 861.10(2) pm,  $c$  = 881.88(2) pm,  $V$  = 566.30(2) · 10<sup>6</sup> pm<sup>3</sup>,  $P6_3cm$  (no. 185),  $Z$  = 6,  $\rho_{calc}$  = 1.76 g cm<sup>-3</sup>,  $\mu$ (Cu K $\alpha$ ) = 7.61 mm<sup>-1</sup>,  $h \leq 7$ ,  $k \leq 7$ ,  $l \leq 8$ ,  $10^\circ \leq 2\theta \leq 90^\circ$ , 4705 points, 32 parameters,  $R_{wp}$  = 0.037,  $R_{exp}$  = 0.023,  $R_p$  = 0.027, GOF = 1.593,  $R_{Bragg}$  = 0.015. Further details of the crystal structure determination are available from the Fachinformationszentrum Karlsruhe, D-76344 Eggenstein-Leopoldshafen, Germany, E-mail: [crysdata@fz-karlsruhe.de](mailto:crysdata@fz-karlsruhe.de), on quoting the depository numbers CSD-433838 (Na<sub>3</sub>P).

**Density Functional Theory and Computational Structure Predictions.** Following the comprehensive structure prediction study of Mayo et al.,<sup>38</sup> a parallel, cross-compositional genetic algorithm (GA) was used to enhance the sampling of metastable Na<sub>3</sub>P phases. Specifically targeting the region  $1 - \delta < x < 2 + \delta$ , new low-lying phases were discovered by extrapolating the local structures found using *ab initio* random structure searching (AIRSS) to larger cells of nontrivial stoichiometries via simple cut-and-splice crossover (70%) and mutation (30%). Aside from physicality of density and bond lengths, two criteria were enforced upon each trial structure; the unit cell must contain fewer than 40 atoms, and it must be unique to other computed structures (as defined via overlap of pair distribution functions). Each trial structure was relaxed with density functional theory (DFT) forces using the planewave pseudopotential code CASTEP (version 16.1)<sup>56</sup> such that formation energies were converged to within 10 meV·atom<sup>-1</sup>. This level of accuracy required a planewave cutoff of 400 eV and a Monkhorst–Pack grid with spacing finer than  $2\pi \times 0.05 \text{ \AA}^{-1}$  to sample the Brillouin zone. The fitness of each structure was evaluated as a logistic function of the distance from the convex hull of previously computed formation energies; fitness proportionate (roulette wheel) selection was used to propagate structures to the next generation, of which 50% were selected from elite structures of earlier generations. Several GA runs were performed with a generation size of 30 relaxed structures, until further generations no longer explored new regions of configuration space.

The 318 unique structures that were found to lie less than 150 meV·atom<sup>-1</sup> from the convex hull were re-relaxed using the exchange–correlation functional of Perdew, Burke, and Ernzerhof (PBE)<sup>57</sup> and Vanderbilt ultrasoft pseudopotentials (generated on-the-fly with Na: 2l 1.3l1.3l1.0l16l19l21l20U:30U:21(qc = 8), P: 2l1.8l1.8l1.5l3l5l6l 30:31:32LGG). Convergence of formation energies to within 1 meV·atom<sup>-1</sup> required truncation of the planewave basis set at 650 eV, and Brillouin zone sampling with a Monkhorst–Pack grid finer than  $2\pi \times 0.03 \text{ \AA}^{-1}$ .<sup>58</sup>

The original work of Mayo et al.<sup>38</sup> searched for candidate crystal structures using a combination of the AIRSS and species-swapping

structure prediction methods. These techniques have been successfully applied in several previous studies of battery materials, such as in Li–Sn and Li–Sb,<sup>51</sup> Na–Sn,<sup>34</sup> and in Li–FeS<sub>2</sub>.<sup>59</sup> As well as the structures arising from our GA searches, we also examined the structures lying within 100 meV·atom<sup>-1</sup> of the convex hull in reference 38 with stoichiometries NaP, Na<sub>2</sub>P, Na<sub>3</sub>P<sub>4</sub>, and Na<sub>5</sub>P<sub>6</sub> for our NMR calculations.

**NMR Calculations.** Chemical shifts and other NMR parameters were calculated using the gauge-including-projector-augmented-wave (GIPAW) algorithm and the Quantum Espresso code,<sup>60</sup> with the GIPAW pseudopotentials Na.pbe-tm-gipaw-dc.UPF and P.pbe-tm-new-gipaw-dc.UPF,<sup>61</sup> and the PBE exchange–correlation functional. A kinetic-energy cutoff of 1360 and 5442 eV was used for the plane-wave expansion of the Kohn–Sham orbitals and the charge density, respectively.

Structures for the NMR calculations were first relaxed using DFT and the CASTEP or Quantum Espresso codes, using a Brillouin zone sampling density of  $2\pi \times 0.025 \text{ \AA}^{-1}$ . Following this, an NMR calculation was carried out with the aforementioned parameters and pseudopotentials using a stricter sampling density of  $2\pi \times 0.008 \text{ \AA}^{-1}$ . With this sampling density, we estimate that total NMR chemical shifts are converged to  $\pm 1$  ppm. We found that this density is necessary as some of our candidate crystal structures display semimetallic or metallic behavior under DFT.

Additional data related to this publication are available at the Cambridge data repository.<sup>62</sup>

## ■ ASSOCIATED CONTENT

### ● Supporting Information

The Supporting Information is available free of charge on the ACS Publications website at DOI: 10.1021/jacs.8b04183.

Additional electrochemistry, solid-state NMR spectroscopy, PXRD, and structural modeling data, including Figures S1–S17 and Tables S1 and S2 (PDF)

## ■ AUTHOR INFORMATION

### Corresponding Authors

\*[a.j.morris.1@bham.ac.uk](mailto:a.j.morris.1@bham.ac.uk)

\*[cpg27@cam.ac.uk](mailto:cpg27@cam.ac.uk)

### ORCID

Lauren E. Marbella: 0000-0003-1639-3913

Matthew L. Evans: 0000-0002-1182-9098

Kent J. Griffith: 0000-0002-8096-906X

Andrew J. Morris: 0000-0001-7453-5698

Clare P. Grey: 0000-0001-5572-192X

### Notes

The authors declare no competing financial interest.

## ■ ACKNOWLEDGMENTS

L.E.M. acknowledges funding from the European Union's Horizon 2020 – European Union research and innovation program under the Marie Skłodowska-Curie grant agreement No. 750294, the Assistant Secretary for Energy Efficiency and Renewable Energy, Office of Vehicle Technologies, of the U.S. DOE under Contract no. DE-AC02-05CH11231, under the Batteries for Advanced Transportation Technologies (BATT) Program subcontract no. 7057154, and the Charles and Katharine Darwin Research Fellowship for support. K.J.G. gratefully acknowledges funding from the Winston Churchill Foundation of the United States and the Herchel Smith Scholarship. M.F.G. is grateful to the Engineering and Physical Sciences Research Council (EPSRC Grant No: EP/P003532/1). M.E. would like to acknowledge the EPSRC Centre for Doctoral Training in Computational Methods for Materials

Science for funding under grant number EP/L015552/1. A.J.M. and J.N. acknowledge the Winton Programme for the Physics of Sustainability. J.N. also acknowledges support from the Isaac Newton Fund. L.E.M. thanks Dr. Derrick Kaseman for providing the Matlab script used to process 2D PASS data. We acknowledge Josh Stratford, Dr. Elizabeth Castillo-Martínez, Dr. Michael Gaultois, Dr. Pieter Magusin, and Prof. Michael Ruck (TU Dresden) for helpful discussions. NMR calculations were performed using the Cambridge Service for Data Driven Discovery (CSD3) operated by the University of Cambridge Research Computing Service (<http://www.csd3.cam.ac.uk/>), provided by Dell EMC and Intel using Tier-2 funding from the Engineering and Physical Sciences Research Council, and DiRAC funding from the Science and Technology Facilities Council ([www.dirac.ac.uk](http://www.dirac.ac.uk)). Structure prediction calculations were performed using the resources of the Center for Functional Nanomaterials, which is a U.S. DOE Office of Science Facility, at Brookhaven National Laboratory under Contract No. DE-SC0012704 and the Thomas Tier 2 facility of the UK national high performance computing service, for which access was obtained via the UKCP consortium and funded by EPSRC grant no. EP/K014560/1.

## REFERENCES

- (1) Choi, J. W.; Aurbach, D. *Nat. Rev. Mater.* **2016**, *1*, 16013.
- (2) Kubota, K.; Komaba, S. *J. Electrochem. Soc.* **2015**, *162*, A2538.
- (3) Kundu, D.; Talaie, E.; Duffort, V.; Nazar, L. F. *Angew. Chem., Int. Ed.* **2015**, *54*, 3431.
- (4) Yabuuchi, N.; Kubota, K.; Dahbi, M.; Komaba, S. *Chem. Rev.* **2014**, *114*, 11636.
- (5) Palomares, V.; Serras, P.; Villaluenga, I.; Hueso, K. B.; Carretero-Gonzalez, J.; Rojo, T. *Energy Environ. Sci.* **2012**, *5*, 5884.
- (6) Dai, Z.; Mani, U.; Tan, H. T.; Yan, Q. *Small Methods* **2017**, *1*, 1700098.
- (7) Xiang, X.; Zhang, K.; Chen, J. *Adv. Mater.* **2015**, *27*, 5343.
- (8) Kang, H.; Liu, Y.; Cao, K.; Zhao, Y.; Jiao, L.; Wang, Y.; Yuan, H. *J. Mater. Chem. A* **2015**, *3*, 17899.
- (9) Bayley, P. M.; Trease, N. M.; Grey, C. P. *J. Am. Chem. Soc.* **2016**, *138*, 1955.
- (10) Cui, J.; Yao, S.; Kim, J.-K. *Energy Storage Materials* **2017**, *7*, 64.
- (11) Kim, Y.; Ha, K.-H.; Oh, S. M.; Lee, K. T. *Chem. - Eur. J.* **2014**, *20*, 11980.
- (12) Luo, W.; Shen, F.; Bommier, C.; Zhu, H.; Ji, X.; Hu, L. *Acc. Chem. Res.* **2016**, *49*, 231.
- (13) Wang, L. P.; Yu, L.; Wang, X.; Srinivasan, M.; Xu, Z. *J. Mater. Chem. A* **2015**, *3*, 9353.
- (14) Dahbi, M.; Yabuuchi, N.; Fukunishi, M.; Kubota, K.; Chihara, K.; Tokiwa, K.; Yu, X.-f.; Ushiyama, H.; Yamashita, K.; Son, J.-Y.; Cui, Y.-T.; Oji, H.; Komaba, S. *Chem. Mater.* **2016**, *28*, 1625.
- (15) Li, W.-J.; Chou, S.-L.; Wang, J.-Z.; Liu, H.-K.; Dou, S.-X. *Nano Lett.* **2013**, *13*, 5480.
- (16) Ramireddy, T.; Xing, T.; Rahman, M. M.; Chen, Y.; Dutercq, Q.; Gunzelmann, D.; Glushenkov, A. M. *J. Mater. Chem. A* **2015**, *3*, 5572.
- (17) Song, J.; Yu, Z.; Gordin, M. L.; Hu, S.; Yi, R.; Tang, D.; Walter, T.; Regula, M.; Choi, D.; Li, X.; Manivannan, A.; Wang, D. *Nano Lett.* **2014**, *14*, 6329.
- (18) Song, J.; Yu, Z.; Gordin, M. L.; Li, X.; Peng, H.; Wang, D. *ACS Nano* **2015**, *9*, 11933.
- (19) Xu, G.-L.; Chen, Z.; Zhong, G.-M.; Liu, Y.; Yang, Y.; Ma, T.; Ren, Y.; Zuo, X.; Wu, X.-H.; Zhang, X.; Amine, K. *Nano Lett.* **2016**, *16*, 3955.
- (20) Zhu, Y.; Wen, Y.; Fan, X.; Gao, T.; Han, F.; Luo, C.; Liou, S.-C.; Wang, C. *ACS Nano* **2015**, *9*, 3254.
- (21) Kim, Y.; Park, Y.; Choi, A.; Choi, N.-S.; Kim, J.; Lee, J.; Ryu, J. H.; Oh, S. M.; Lee, K. T. *Adv. Mater.* **2013**, *25*, 3045.
- (22) Sun, J.; Lee, H.-W.; Pasta, M.; Yuan, H.; Zheng, G.; Sun, Y.; Li, Y.; Cui, Y. *Nat. Nanotechnol.* **2015**, *10*, 980.
- (23) Nitta, N.; Lei, D.; Jung, H.-R.; Gordon, D.; Zhao, E.; Gresham, G.; Cai, J.; Luzinov, I.; Yushin, G. *ACS Appl. Mater. Interfaces* **2016**, *8*, 25991.
- (24) Sun, J.; Zheng, G.; Lee, H.-W.; Liu, N.; Wang, H.; Yao, H.; Yang, W.; Cui, Y. *Nano Lett.* **2014**, *14*, 4573.
- (25) Wang, L.; He, X.; Li, J.; Sun, W.; Gao, J.; Guo, J.; Jiang, C. *Angew. Chem., Int. Ed.* **2012**, *51*, 9034.
- (26) Wang, L.; Zhou, Z.; Li, J.; He, X. *Ionics* **2018**, *24*, 303.
- (27) Bai, A.; Wang, L.; Li, J.; He, X.; Wang, J.; Wang, J. *J. Power Sources* **2015**, *289*, 100.
- (28) Yue, Z.; Gupta, T.; Wang, F.; Li, C.; Kumar, R.; Yang, Z.; Koratkar, N. *Carbon* **2018**, *127*, 588.
- (29) Tojo, T.; Yamaguchi, S.; Furukawa, Y.; Aoyanagi, K.; Umezaki, K.; Inada, R.; Sakurai, Y. *J. Electrochem. Soc.* **2018**, *165*, A1231.
- (30) Michan, A. L.; Divitini, G.; Pell, A. J.; Leskes, M.; Ducati, C.; Grey, C. P. *J. Am. Chem. Soc.* **2016**, *138*, 7918.
- (31) Mortazavi, M.; Ye, Q.; Biribilis, N.; Medhekar, N. V. *J. Power Sources* **2015**, *285*, 29.
- (32) Radvanyi, E.; Porcher, W.; De Vito, E.; Montani, A.; Franger, S.; Jouanneau Si Larbi, S. *Phys. Chem. Chem. Phys.* **2014**, *16*, 17142.
- (33) Zhang, W.-J. *J. Power Sources* **2011**, *196*, 13.
- (34) Stratford, J. M.; Mayo, M.; Allan, P. K.; Pecher, O.; Borkiewicz, O. J.; Wiaderek, K. M.; Chapman, K. W.; Pickard, C. J.; Morris, A. J.; Grey, C. P. *J. Am. Chem. Soc.* **2017**, *139*, 7273.
- (35) Allan, P. K.; Griffin, J. M.; Darwiche, A.; Borkiewicz, O. J.; Wiaderek, K. M.; Chapman, K. W.; Morris, A. J.; Chupas, P. J.; Monconduit, L.; Grey, C. P. *J. Am. Chem. Soc.* **2016**, *138*, 2352.
- (36) Sottmann, J.; Di Michiel, M.; Fjellvåg, H.; Malavasi, L.; Margadonna, S.; Vajeeston, P.; Vaughan, G. B. M.; Wragg, D. S. *Angew. Chem., Int. Ed.* **2017**, *56*, 11385.
- (37) Duer, M. J. *Solid state NMR spectroscopy: principles and applications*; John Wiley & Sons: Oxford, 2002.
- (38) Mayo, M.; Griffith, K. J.; Pickard, C. J.; Morris, A. J. *Chem. Mater.* **2016**, *28*, 2011.
- (39) Jung, H.; Allan, P. K.; Hu, Y.-Y.; Borkiewicz, O. J.; Wang, X.-L.; Han, W.-Q.; Du, L.-S.; Pickard, C. J.; Chupas, P. J.; Chapman, K. W.; Morris, A. J.; Grey, C. P. *Chem. Mater.* **2015**, *27*, 1031.
- (40) Grotz, C.; Köpf, M.; Baumgartner, M.; Jantke, L. A.; Raudaschl-Sieber, G.; Fässler, T. F.; Nilges, T. Z. *Anorg. Allg. Chem.* **2015**, *641*, 1395.
- (41) Koch, V. R.; Young, J. H. *Science* **1979**, *204*, 499.
- (42) Brauer, G.; Zintl, E. *Z. Phys. Chem.* **1937**, *37B*, 323.
- (43) Dong, Y.; DiSalvo, F. J. *Acta Crystallogr., Sect. E: Struct. Rep. Online* **2005**, *61*, i223.
- (44) Hafner, P.; Range, K.-J. *J. Alloys Compd.* **1994**, *216*, 7.
- (45) Kaseman, D. C.; Gulbitten, O.; Aitken, B. G.; Sen, S. *J. Chem. Phys.* **2016**, *144*, 174501.
- (46) Massiot, D.; Fayon, F.; Capron, M.; King, I.; Le Calvé, S.; Alonso, B.; Durand, J.-O.; Bujoli, B.; Gan, Z.; Hoatson, G. *Magn. Reson. Chem.* **2002**, *40*, 70.
- (47) Hembram, K. P. S. S.; Jung, H.; Yeo, B. C.; Pai, S. J.; Kim, S.; Lee, K.-R.; Han, S. S. *J. Phys. Chem. C* **2015**, *119*, 15041.
- (48) Georg, H.; Schnering, V.; Hönle, W. Z. *Anorg. Allg. Chem.* **1979**, *456*, 194.
- (49) Courtney, I. A.; Dahn, J. R. *J. Electrochem. Soc.* **1997**, *144*, 2045.
- (50) Key, B.; Morcrette, M.; Tarascon, J.-M.; Grey, C. P. *J. Am. Chem. Soc.* **2011**, *133*, 503.
- (51) Mayo, M.; Morris, A. J. *Chem. Mater.* **2017**, *29*, 5787.
- (52) Antzutkin, O. N.; Shekar, S. C.; Levitt, M. H. *J. Magn. Reson., Ser. A* **1995**, *115*, 7.
- (53) Harris, R. K.; Becker, E. D.; Cabral de Menezes, S. M.; Granger, P.; Hoffman, R. E.; Zilm, K. W. *Pure Appl. Chem.* **2008**, *80*, 59.
- (54) Coelho, A. *Topas 4.1*; Coelho Software: Brisbane, Australia, 2007.
- (55) Brandenburg, K. *Diamond 3.2k, Crystal and Molecular Structure Visualization*; Crystal Impact GbR: Bonn, Germany, 1999.



- (56) Clark, S. J.; Segall, M. D.; Pickard, C. J.; Hasnip, P. J.; Probert, M. I. J.; Refson, K.; Payne, M. C. *Z. Kristallogr. - Cryst. Mater.* **2005**, *220*, 567.
- (57) Perdew, J. P.; Burke, K.; Ernzerhof, M. *Phys. Rev. Lett.* **1996**, *77*, 3865.
- (58) Monkhorst, H. J.; Pack, J. D. *Phys. Rev. B* **1976**, *13*, 5188.
- (59) Butala, M. M.; Mayo, M.; Doan-Nguyen, V. V. T.; Lumley, M. A.; Göbel, C.; Wiaderek, K. M.; Borkiewicz, O. J.; Chapman, K. W.; Chupas, P. J.; Balasubramanian, M.; Laurita, G.; Britto, S.; Morris, A. J.; Grey, C. P.; Seshadri, R. *Chem. Mater.* **2017**, *29*, 3070.
- (60) Giannozzi, P.; Baroni, B.; Bonini, B.; Calandra, C.; Car, C.; et al. *J. Phys.: Condens. Matter* **2009**, *21*, 395502.
- (61) Ceresoli, D. Pseudopotentials, <https://sites.google.com/site/dceresoli/pseudopotentials>.
- (62) Marbella, L. E.; Evans, M.; Groh, M. F.; Nelson, J.; Griffith, K.; Morris, A.; and Grey, C. P. Research data supporting: “(De)Sodiation via Helical Phosphorus Intermediates in High Capacity Anodes for Sodium-ion Batteries”, <https://doi.org/10.17863/CAM.16738>.